



# Void Lensing in Cubic Galileon Gravity

Chen Su<sup>1,2</sup>, Huanyuan Shan<sup>1,2</sup> , Jiajun Zhang<sup>1,2</sup> , Cheng Zhao<sup>3,4</sup>, Jiaxi Yu<sup>4</sup>, Qiao Wang<sup>2,3</sup>, Linfeng Xiao<sup>5</sup>, Xiangkun Liu<sup>6</sup>, and An Zhao<sup>6</sup>

<sup>1</sup> Shanghai Astronomical Observatory (SHAO), Nandan Road 80, Shanghai, 200030, People's Republic of China; [suchen@shao.ac.cn](mailto:suchen@shao.ac.cn), [hyshan@shao.ac.cn](mailto:hyshan@shao.ac.cn), [jjzhang@shao.ac.cn](mailto:jjzhang@shao.ac.cn)

<sup>2</sup> University of Chinese Academy of Sciences, Beijing, 100049, People's Republic of China

<sup>3</sup> National Astronomy Observatories, Chinese Academy of Science, Beijing, 100101, People's Republic of China

<sup>4</sup> Laboratory of Astrophysics, École Polytechnique Fédérale de Lausanne (EPFL), Observatoire de Sauverny, CH-1290 Versoix, Switzerland

<sup>5</sup> Department of Physics and Astronomy, Sejong University, Seoul, 143-747, Republic of Korea

<sup>6</sup> South-Western Institute for Astronomy Research, Yunnan University, Kunming, 650500, People's Republic of China

Received 2022 November 26; revised 2023 May 13; accepted 2023 May 15; published 2023 July 4

## Abstract

Weak-lensing studies via cosmic voids are a promising probe of modified gravity (MG). The excess surface mass density (ESD) is widely used as a lensing statistic in weak-lensing research. In this paper, we use the ray-tracing method to study the ESD around voids in simulations based on cubic Galileon (CG) gravity. With the compilation of an  $N$ -body simulation and the ray-tracing method, changes in structure formation and deflection angle resulting from MG can both be considered, making the extraction of lensing signals more realistic. We find good agreements between the measurement and theoretical prediction of ESD for CG gravity. However, the lensing signals are much less affected by the change in the deflection angle than by the change in the structure formation, indicating a good approximation of the ESD (statistics) as the projection of the 3D dark matter density field. Finally, we demonstrate that it is impossible to distinguish CG and general relativity in our simulation, but in the next-generation survey, thanks to the large survey area and the increased galaxy number density, detecting the differences between these two models is possible. The method employed in this paper, which combines an  $N$ -body simulation and the ray-tracing method, can be a robust way to measure the lensing signals from simulations based on the MGs, and especially on that which significantly modifies the deflection angle.

*Unified Astronomy Thesaurus concepts:* Weak gravitational lensing (1797); Cosmology (343); Voids (1779); Non-standard theories of gravity (1118)

## 1. Introduction

The discovery of the late-time acceleration of the Universe brings us a new view of the components in the Universe. In the framework of general relativity (GR), approximately 70% of the total energy in our Universe is occupied by dark energy, a component that could be mimicked by a cosmological constant,  $\Lambda$ , but the exact nature of which is currently unclear. On the other hand, the expanded Universe may suggest the need for new physics beyond the framework of Einstein's theory, which motivates the study of modified gravity (MG). Without the cosmological constant, these theories propose several alternatives to GR to explain the accelerating Universe.

Cubic Galileon (CG) theory, a special (and simple) case of Horndeski theory (Horndeski 1974; Kobayashi 2019), is one of the scalar-tensor theories that allows a modification of GR through a scalar field  $\phi$ . “Galileon” means that the Lagrangian of the theory is invariant under the transformation  $\phi \rightarrow \phi + b_\mu x^\mu + c$ , and “cubic” refers to the highest order of three in terms of  $\phi$ . Previous works have studied the properties of cubic and higher-order Galileon theories (de Felice & Tsujikawa 2010; Nesseris et al. 2010; de Felice et al. 2011; Barreira et al. 2013a, 2013b, 2013c; Renk et al. 2017), including linear perturbations and nonlinear structure formations. Most of them consider a “kinetic essence” case, i.e., they ignore the first term, a potential term of the Lagrangian of the

Galileon theory. In other words, in these studies, the acceleration of the Universe is driven by the kinetic term. However, it is difficult to induce a stable late-time acceleration for CG without the potential term (Gannouji & Sami 2010; Zhang et al. 2020). The constraint on the gravitational wave propagation speed from the events of binary neutron star merger (Abbott et al. 2017a, 2017b, 2017c) has ruled out a large class of Horndeski models (Ezquiaga & Zumalacárregui 2017; Zumalacárregui 2020), however, including Galileon theories with terms whose order of the Galileon field  $\phi$  is higher than three. Therefore, investigating a CG model with a potential term is more realistic for a comparison with observations.

There are many difficulties in distinguishing MG theories from GR. One of them is the screening mechanism, which suppresses the deviations from GR in high-density or small-scale regions due to the great success of GR in these environments. There are mainly two types of screening mechanisms. The first is called the chameleon mechanism (Khouri & Weltman 2004a, 2004b). It suppresses the observational effects of MGs in high-density regions where the Newtonian potential is deep enough. The other is the Vainshtein mechanism (Vainshtein 1972; Babichev & Delfayet 2013). It appears in CG theory and introduces high-order derivative interactions to suppress modification terms on small scales. These mechanisms allow MGs to pass local tests in the solar system, but prevent us from distinguishing them from GRs in these regions.

In contrast, cosmic voids, the underdense regions in large-scale structures, provide a special environment to explore the



Original content from this work may be used under the terms of the [Creative Commons Attribution 4.0 licence](https://creativecommons.org/licenses/by/4.0/). Any further distribution of this work must maintain attribution to the author(s) and the title of the work, journal citation and DOI.

differences between GR and MG theories. Due to the properties of an underdensity and large scales, voids are less influenced by the chameleon and Vainshtein mechanisms, making them an ideal probe for testing MG theories. For instance, Cai et al. (2015), Perico et al. (2019), and Davies et al. (2019) have examined several void properties, such as the void abundance, the void density profile, and the void lensing profiles in MG theories. Cautun et al. (2018) and Paillas et al. (2019) have investigated these properties of voids on chameleon-screened and Vainshtein-screened gravity theories, respectively, but focused on the differences between various void finders. Several works have used a single property of a void to test a special MG theory. For example, Barreira et al. (2015) and Baker et al. (2018) focused on void lensing in CG theory; Barreira et al. (2017) also focused on void lensing, but for the normal branch of Dvali–Gabadadze–Porrati braneworld theory, and Wilson & Bean (2021) used the void velocity profile to test  $f(R)$  gravity. For a special case, Cataldi et al. (2022) studied the properties of galaxies in voids and observed some fingerprints of the  $f(R)$  theory. Results from these researches support that a void is a useful tool for studying and testing MG theories with screen mechanisms.

Weak lensing by cosmic voids is a powerful tool for testing gravity. Observationally, weak-lensing effects can be detected by measuring the distortion of the shape of background galaxies. Thus, it is convenient to compare lensing effects between theory and observation/simulation. From a theoretical perspective, lensing signals are sensitive to the lensing potential, which is directly influenced by modifications of gravity. This makes weak lensing a good probe of deviations from GR. In MGs, lensing signals can be influenced by both the dark matter distribution<sup>7</sup> and the deflection angle, which has been observed in the literature for a long time (Barreira et al. 2015, 2017; Baker et al. 2018; Cai 2018) and is always considered in theoretical calculations. Nevertheless, when measuring lensing signals from simulations, the case becomes more complex. In GR, the lensing convergence can directly represent the distribution of matter density, as there is a linear relation between the second derivative of Newtonian potential and matter density. This coincidence brings the viewpoint that the lensing tangential shear (obtained by differentiating the convergence) represents the excess surface mass density. By projecting the 3D dark matter density from  $N$ -body simulation, one can obtain the tangential shear signals. However, in most MG theories, the relation between Newtonian potential and matter density is no longer linear, breaking the coincidence. Therefore, the lensing signal cannot be obtained from the projected differential mass density as it does not account for the effect due to the modification of the deflection angle.

In this work, we employ ray-tracing methods to analyze the lensing signals around voids in the context of CG theory. With the ray-tracing simulation results, the (mock) source galaxy shear catalog can be constructed. Combining this with the lens void catalog, we can measure the lensing signals around the voids. Our method has several advantages compared with

previous works, including the consideration of modifications to both the structure formation and the deflection angle (compared with directly projecting the 3D density profile), and the full contributions from the matter between the source plane and the observer (compared with cutting part of the region near the lens objects). In this sense, our results are more reliable, motivating the first aim of this work, which is to investigate whether these two approximate strategies are valid for CG theory. One other aim of this work is to test the possibility (and if possible, capability) of void lensing in distinguishing CG and GR.

The structure of the paper is as follows: in Section 2 we briefly introduce the theory investigated in this work, which contains the gravity model and basic equations in the lensing calculation. In Section 3 we introduce our simulation information, in which the void properties used in the following section are also described and discussed. In Section 4 we present our main results, including theoretical calculations and the simulation results. The capability of void lensing to distinguish MG models is also discussed in this section. Section 5 contains the summary and conclusions of this paper.

## 2. Theory

In this section, we outline the theoretical framework employed in this work. First, we present the basic theory of the cubic Galileon gravity model, then we generally describe the calculation procedure of the lensing signal. At the end of this section, we discuss the subtleties of the lensing statistics,  $\Delta\Sigma$ , illustrating that it may not be the physical surface mass density in MG theories. The following discussion is based on the perturbed Friedmann–Robertson–Walker (FRW) metric with the Newtonian gauge

$$ds^2 = -(1 + 2\Psi)dt^2 + a^2(t)(1 - 2\Phi)\gamma_{ij}dx^i dx^j, \quad (1)$$

where  $a = 1/(1+z)$  is the scale factor with the redshift  $z$ . The background FRW metric satisfies  $\Phi = \Psi = 0$ .

### 2.1. Gravity Model

Galileon theory modifies GR by introducing a scalar field,  $\phi$ , with its unusual high-order derivative self-interaction (Nicolis et al. 2009). The action of Galileon gravity is

$$S = \int d^4x \sqrt{-g} \left[ \frac{M_{\text{pl}}^2}{2} R - \frac{1}{2} (\nabla\phi)^2 (1 + \beta \square\phi) - V(\phi) \right] + S_m, \quad (2)$$

where  $M^3 = M_{\text{pl}} H_0^2$ ,  $M_{\text{pl}} = 1/\sqrt{8\pi G}$  is the reduced Planck mass. The variation of the action with respect to the metric tensor  $g_{\mu\nu}$  in flat FRW metric leads to two background Friedmann equations,

$$3M_{\text{pl}}^2 H^2 = \bar{\rho}_m + \frac{\dot{\phi}^2}{2} (1 - 6\beta H \dot{\phi}) + V(\phi) \quad (3)$$

$$M_{\text{pl}}^2 (2\dot{H} + 3H^2) = -\frac{\dot{\phi}^2}{2} (1 + 2\beta \ddot{\phi}) + V(\phi). \quad (4)$$

The equation of motion of the Galileon field  $\phi$  can be derived by varying the action with respect to  $\phi$ . We split the full Galileon field  $\phi$  into a homogeneous part  $\bar{\phi}$  and a perturbed

<sup>7</sup> In this work, we do not consider the baryon effect, and therefore, effects due to the change in the structure formation directly result in differences of the dark matter field between two gravity models. In this work, we focus on void lensing, where voids are chosen as the tracer of dark matter. Therefore, the change in the dark matter field causes different void density profiles. In this paper, different expressions are used to describe this effect: the change in the structure formation, the change in the dark matter field, and the change in the void profile, and we point out that these are all equivalent.

part  $\varphi$ . In flat FRW metric, the equation of motion of  $\bar{\phi}$  reads

$$\ddot{\bar{\phi}} + 3H\dot{\bar{\phi}} - 3\bar{\phi}\dot{(3H^2\bar{\phi} + \dot{H}\bar{\phi} + 2H\ddot{\bar{\phi}})} + V_{\bar{\phi}} = 0, \quad (5)$$

where overdots represent derivations with physical time, and  $V_{\bar{\phi}}$  represents the derivation with respect to  $\bar{\phi}$ . Using a set of dimensionless quantities to replace the variables in Equations (4) and (5), these equations can be solved numerically (Hossain & Sen 2012; Zhang et al. 2020). The initial value of one of the dimensionless quantities,  $\epsilon = -6\beta H^2\phi'$ , where a prime represents the derivative with respect to the number of e-foldings  $N \equiv \ln(a)$ , can be chosen as a free parameter. However, in this work, we fix this free parameter  $\epsilon_i$  and regard the CG theory as a model without any free parameters, leaving constraining the parameter to future work. We choose  $\epsilon_i = 0$  because in this case, CG and GR universes present the most distinct properties.

Furthermore, it is necessary to perform perturbation calculations because the lensing signal is sensitive to the perturbation quantities in the metric tensors. Varying the action Equation (2) with respect to the metric and the Galileon field and in the perturbed FRW metric Equation (1) we can obtain the perturbed Einstein equations as well as the equation of the motion of the perturbed Galileon field  $\delta\varphi$  up to the first order. These tedious equations can be found in Zhang et al. (2020) and are not shown here. Finally, on the strength of the evolution of  $\Phi$  and the perturbed metric potentials, we are able to calculate the lensing signal.

## 2.2. Weak-lensing Signal

The weak-lensing effect is caused by light bending by foreground objects or structures. This effect can cause the distortion of the shapes of background galaxies, which can be quantified by the tangential shear  $\gamma_t$ . It is related to the lensing convergence,  $\kappa$ , by

$$\gamma_t = \bar{\kappa} - \kappa, \quad (6)$$

where  $\bar{\kappa}$  represents the mean convergence in a given radius,  $\bar{\kappa}(<R) = \int_0^R r\kappa(r)dr$ .

Theoretically,  $\kappa$  is half of the second derivation of the lensing potential (Schneider 2006), which is the integral of the sum of the metric potentials, i.e., lensing potential,

$$\kappa = \frac{1}{2}\nabla^2\psi_{\text{lens}} = \frac{1}{4\pi G\Sigma_{\text{crit}}} \int \frac{1}{2}\nabla^2(\Phi + \Psi)d\ell, \quad (7)$$

where  $\Sigma_{\text{crit}}$  is the geometry factor dependent on the lens system.  $\ell$  represents the comoving distance along the line of sight. For GR,  $\Phi = \Psi$ , and by using the Poisson equation,  $\nabla^2\Phi = 4\pi G a^2 \rho_m \delta$ , Equation (7) can be expressed as

$$\begin{aligned} \kappa &= \frac{1}{4\pi G\Sigma_{\text{crit}}} \int 4\pi G a^2 \rho_m \delta d\ell \\ &= \frac{\bar{\rho}_{m0}}{\Sigma_{\text{crit}}} \int \frac{\delta}{a} d\ell = \frac{\bar{\rho}_{m0}}{\Sigma_{\text{crit},c}} \int \delta d\ell, \end{aligned} \quad (8)$$

where for the second line, we use  $\rho_m = \bar{\rho}_{m0}a^{-3}$ .  $\Sigma_{\text{crit}}$  and  $\Sigma_{\text{crit},c}$  represent the geometry factor expressed in physical and comoving coordinates, respectively. Note that  $\Sigma_{\text{crit}}$  has the meaning of surface mass, thus, analogous to the critical density  $\bar{\rho}_m$ , with the expansion of the Universe,  $\Sigma_{\text{crit}}$  should be

inversely proportional to  $a^{-2}$ . In other words, the relation of the expression of  $\Sigma_{\text{crit}}$  in physical coordinates and in comoving coordinates is  $\Sigma_{\text{crit}} = \Sigma_{\text{crit},c} \times a^{-2}$  (Amon et al. 2018).

For CG, there is no anisotropic stress, i.e.,  $\Phi = \Psi$ , but  $\Phi_{\text{CG}} \neq \Phi_{\text{GR}}$ . In this case, we rewrite the Poisson equation as  $-k^2\Phi = 4\pi a^2 G_{\text{eff}}(k, a)\delta\rho_k$ , and we first apply a Fourier transform on the void density profile to obtain  $\rho_k$ , then we calculate  $-k^2\Phi$ , and finally, we apply an inverse Fourier transformation to obtain  $\nabla^2\Phi$ .

With the convergence  $\kappa$ , the excess surface mass density (ESD) can be given as

$$\Delta\Sigma = \Sigma_{\text{crit},c}(\bar{\kappa} - \kappa). \quad (9)$$

From Equation (9) we can see that the calculation of  $\Sigma_{\text{crit},c}$  can be avoided. The only ingredient needed in the calculation is the density profile of the foreground objects, i.e., the void density profile in this work. Instead of using a fitting function, we directly use the profile from the  $N$ -body simulation because the void profiles in the two gravity models are very similar (Cautun et al. 2018). Details of the void profile can be found in Section 3.

## 2.3. Discussion of the ESD

At the end of this section, we aim to provide a discussion of the ESD,  $\Delta\Sigma$ , a commonly used statistics for studying weak-lensing effects in the literature (Melchior et al. 2014; Barreira et al. 2015; Cai et al. 2015; Clampitt & Jain 2015). It should be noted that as a lensing statistic,  $\Delta\Sigma$  may not have the physical meaning of excess surface mass density. The original definition of the surface mass density is simply the integral of the volume density in one dimension,  $\Sigma = \int \rho d\ell$ . In GR, the integral part of Equation (7) is equivalent to the surface mass density by coincidence because the second deviation of the Newtonian potential is proportional to the volume density. However, in MGs, one needs to subtract the effects from the modified theory when calculating the (real) surface mass density from the lensing statistics  $\Delta\Sigma$ . For instance, in a certain MG theory where the Poisson equation reads  $\nabla^2\Phi_{\text{MG}} = 4\pi G\rho + \mathcal{M}$ , the surface mass density should be expressed as  $\Sigma = (1/4\pi G) \int (\nabla^2\Phi_{\text{MG}} - \mathcal{M})d\ell$  rather than  $\Sigma = (1/4\pi G) \int \nabla^2\Phi_{\text{MG}}d\ell$ , in order to be consistent with its original definition. Therefore, directly projecting the 3D dark matter density may not induce the correct lensing signal. To this end, we employ the ray-tracing algorithm to simulate the observed convergence map and shear map in the scenario of CG, and measure the lensing signal directly from the simulation results. Certainly, one salient advantage of this approach is its independence on the gravity framework in which one works, implying its flexible usage in any MG theory.

## 3. Simulation

In this section, we describe the ingredients necessary for the theoretical calculation and measurement of the lensing signal. Specifically, we require the density profile of the foreground void as input, as well as the background shear and foreground void catalogs for the measurements. We begin by introducing our  $N$ -body simulation and subsequently construct the void catalog. Next, we measure the void density profiles in both gravity models. Finally, we provide a detailed description of our ray-tracing method, which enables us to obtain the



observed convergence and shear maps from the simulated void and matter density fields.

### 3.1. N-body Simulation

We use the ME-GADGET code (Zhang et al. 2018, 2020) to generate a simulation of  $512^3$  particles in a periodic box whose size is  $L = 400 \text{ Mpc h}^{-1}$  for the GR and CG simulations, with a softening length of  $25 \text{ kpc h}^{-1}$ . The initial condition is generated with 2LPTic (Crocce et al. 2006), while the pre-initial condition file is generated by CCVT (Liao 2018). For the GR case, we assume a flat  $\Lambda$ CDM model with a cosmological parameter set of  $\{\Omega_{m0}, \Omega_{b0}, h, \sigma_8, n_s\} = \{0.3156, 0.0491, 0.6727, 0.831, 1.0\}$ . For the CG case, we choose  $\epsilon_i = 0$ , which is the case most different from GR. We store 11 snapshots from  $z = 0$  to  $z = 1$  with a redshift interval of  $\Delta z = 0.1$ , which are used to generate the backward light cones in the next step. In order to reduce the cosmic variance in the following measurements, for each gravity model, we keep the cosmological parameters the same, but change the random seeds to generate 10 realizations and average the results obtained from those simulations.

### 3.2. Void Catalog and Density Profile

In this work, we rely on the Delaunay triangulation void finder (DIVE; Zhao et al. 2016) to identify voids from galaxy samples. First, we generate the halo catalogs from  $N$ -body simulation by using AHF halo finder (Knollmann & Knebe 2011). We then apply the subhalo abundance matching (SHAM) method on the simulations to generate realistic mock galaxies that reproduce the observed clustering, thus providing a good sample to find voids as the lenses in the foreground. SHAM assigns galaxies to halos or subhalos based on the assumption of a monotonic galaxy luminosity–halo mass relation (Kravtsov et al. 2004; Behroozi et al. 2010). We generate mock galaxies with an effective redshift  $z_{\text{eff}} = 0.3$ , as the redshift of lens mocks is sufficiently distant from the source to produce a significant lensing signal. The SHAM algorithm used in this work is described in Yu et al. (2022). We fit the two-point correlation function of the SHAM galaxy catalog to that of the BOSS LOWZ samples at  $0.2 < z < 0.33$ . As we have 10 realizations of the  $N$ -body simulation, we apply the same parameter set to all realizations and average their output 2PCFs to obtain the best-fit SHAM parameters. The parameter set with the maximum likelihood is then implemented on all the realizations to generate the corresponding galaxy mocks with the same cosmology. Finally, we run DIVE on the SHAM galaxy samples to generate void catalogs. We divide the voids into eight size bins based on their radius, ranging from  $R_v = 15 \text{ Mpc h}^{-1}$  to  $R_v = 25 \text{ Mpc h}^{-1}$ . The interval of the first six bins is  $1 \text{ Mpc h}^{-1}$ , while the last two bins have intervals of  $2 \text{ Mpc h}^{-1}$  because the number of voids with radius  $R_v > 21 \text{ Mpc h}^{-1}$  is too small. Voids within the same size bin are assigned the same effective radius, defined by the median of the edge of the bin. For example, voids within the size bin of  $15 \text{ Mpc h}^{-1} < R_v < 16 \text{ Mpc h}^{-1}$  are assigned the same effective radius  $R_{\text{veff}} = 15.5 \text{ Mpc h}^{-1}$ . Figure 1 displays the void number distribution with respect to the radius ( $dN/dR$ ) in simulations under GR and CG gravity, respectively, illustrating that the distributions of void radii are quite similar in both gravity models. These voids are regarded as lenses in the measurements of ESD in the subsequent section.

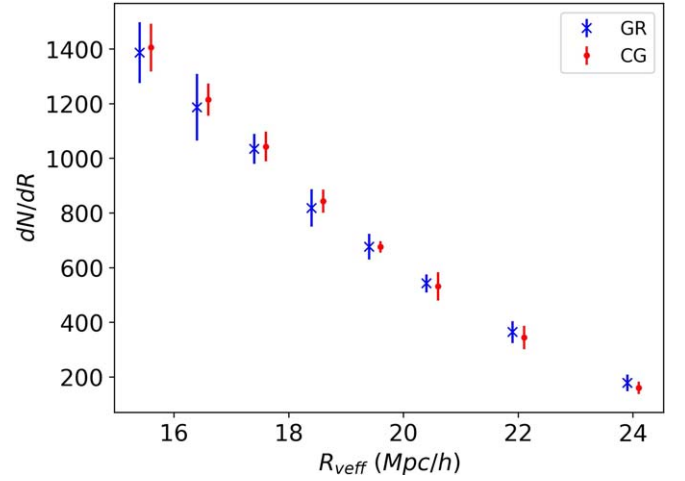


**Figure 1.** The void-size function in two gravity models. The red dots represent GR voids, and the blue crosses represent CG voids. The error bar represents the sample variance. It can be seen that voids in the two simulations have a similar radius distribution.

Void profiles are measured by cross-correlating the position of the center of voids and the dark matter particles, which can be estimated through pair counts, i.e., histograms binned by pair separations (Zhao et al. 2022). We use a simple estimator,

$$\hat{\xi}_{vm} = \frac{DD}{RR} - 1, \quad (10)$$

where  $D$  and  $R$  represent the data and random catalog, respectively. In this work, data refer to the catalog in simulations. To increase the number of voids for measuring the void lensing signal, we stack those voids with different effective radii. Practically, we rescale the coordinates of the tracers using the void effective radii and measure the pair counts as a function of rescaled distance. Because voids with different effective radius should be assigned by different rescaled values, we measure the pair counts separately for the eight size bins and obtain eight sets of results. These pair counts are then added up to construct total pair counts. Finally, we estimate the void-dark matter cross-correlation function using these total pair counts. The fast correlation function calculator (FCFC; Zhao et al. 2021) is used to measure the pair counts in individual size bins.

We average over the void profiles measured from nine realizations for the GR and CG cases, shown in Figure 2. Only three radius size bins in the left panel are presented for the sake of clarity. The right panel shows the stacked void profile, where only the voids with a radius greater than  $18 \text{ Mpc h}^{-1}$  are stacked because the lensing signals around these voids are stronger. The differences in void profiles (relative to GR) are shown in the lower panels. From the left panel, one can see that the CG voids in all three size bins are slightly emptier than the GR voids, inferring the same characteristics in the lensing profile. It is also clear from the left panel of Figure 2 that voids with different sizes present different profile shapes. The larger the void, the emptier it is. Smaller voids tend to have a higher well near the radius of  $r = R_{\text{veff}}$ . The profile of the stacked voids exhibits a smoother shape, both for the GR and CG voids, as can be seen in the right panel of Figure 2. Additionally, we observe a local valley at  $r \sim 1.1 R_{\text{veff}}$ . However, combined with the length of the error bar, these

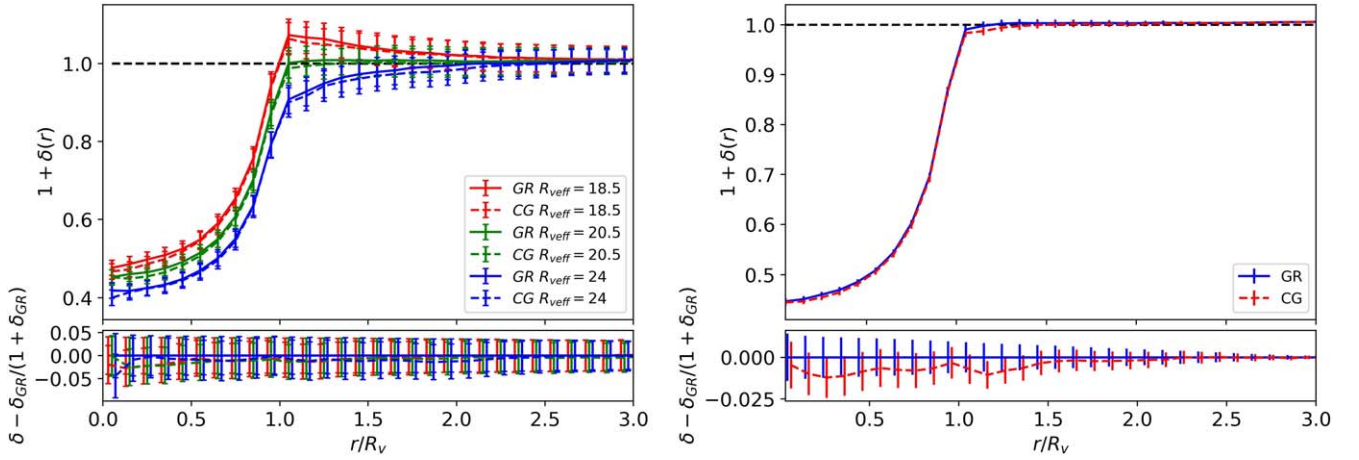


**Figure 2.** Void profiles as a function of the rescaled distance to the void center,  $r/R_v$ . Note that data points in the bottom panel are shifted for clarity. Left: Void density profiles for three void-size bins:  $18 < R_v < 19$ ,  $20 < R_v < 21$ , and  $23 < R_v < 25$ . The solid lines represent the GR void profiles, and the dashed lines represent the CG void profiles. One color represents one void-size bin. The error bars are estimated by jackknife technique. It is obvious that voids of different sizes have different properties in density profile. However, the differences between gravity models are not statistically significant. Right: Stacked void profile in two gravity models. The dashed red line represents the stacked CG void profile, and the solid blue line represents the stacked GR void profile. The error bar is propagated from the jackknife error in a single simulation during the averaging of the void profile. One can see that the deviation between the two models is much smaller than in voids in a narrow size bin, and it is also not statistically significant.

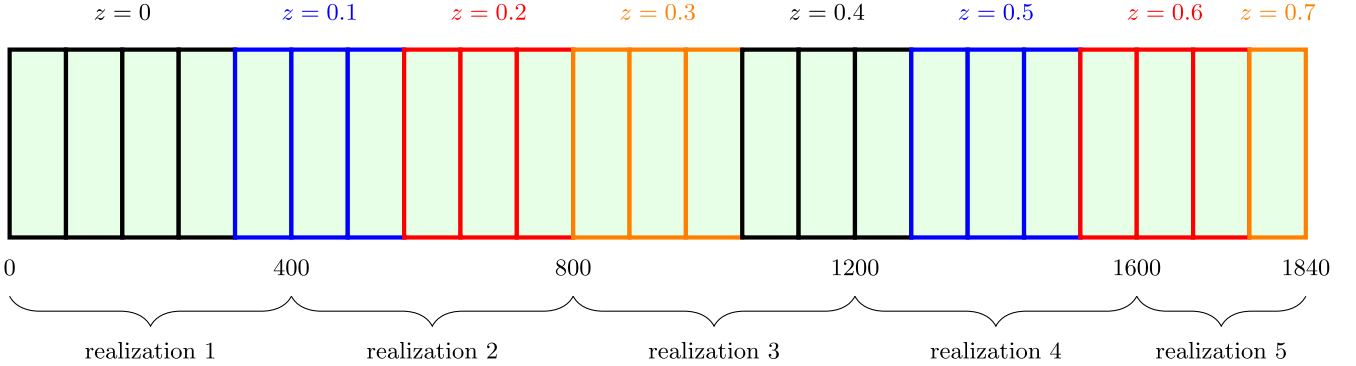


**Figure 3.** A schematic diagram of the light cone. Each rectangle represents a slice. The colors of the slices represent the redshifts of snapshots used to fill the slice. The comoving distances for the edges of slices are given in  $\text{Mpc } h^{-1}$ . We also mark the realizations used in constructing the light cone.

differences are not significant statistically. These void profiles are used in the theoretical calculations of the ESD in the next section. In the last part of the paper, we use  $R_v$  to represent the effective radius  $R_{\text{eff}}$ .

### 3.3. Ray-tracing Algorithm

We trace the light rays from  $z_{\text{source}} = 0.75$  to  $z_{\text{obs}} = 0$ , corresponding to a comoving distance of  $d \approx 1840 \text{ Mpc } h^{-1}$ , and the simulated area is about  $12.45 \times 12.45 \text{ deg}^2$ . Our ray-tracing algorithm is mainly based on Hilbert et al. (2009), and we briefly outline the main steps here. The backward light cone is divided into 23 redshift slices, the width of each of which is of  $\ell = 80 \text{ Mpc } h^{-1}$ . Since the slice width is smaller than the box size, we take every three slices from one snapshot, except for the first four and the last one. To avoid encountering the same structures many times along the line of sight, we change the realization of the snapshot every five slices (i.e., a total width equal to the box size of our simulation). A schematic diagram of the light cone is illustrated in Figure 3. We construct nine different light cones by taking turns using the 10  $N$ -body simulations, then employ the ray-tracing method on these light cones. Finally, we average the measurements from these ray-tracing results to reduce the cosmic variance.

After constructing the light cone, the lens planes are generated by projecting the particles in slices along the line of sight. The comoving distance of each lens plane is determined by the redshift of the corresponding slice. The matter density field is then constructed using the particle-mesh (PM) method, which is used to compute the gravitational potential. Finally, the deflection angle and the corresponding quantities, such as lensing convergence and shear, can be calculated straightforwardly. For CG, the Poisson equation can be rewritten as  $-k^2\Phi = 4\pi G_{\text{eff}}(k, z)\delta\rho_m$ , and in principle, we can replace the constant  $G$  with  $G_{\text{eff}}$  when calculating the deflection angle. However, because  $G_{\text{eff}}$  is very close to the gravitational constant  $G$ , we choose a simpler way to test the influences of the modification to the Poisson equation. First, we determine the maximum value of  $G_{\text{eff}}$  in the range of  $k$  and  $z$  of interest. Then, the original gravitational constant  $G$  is directly replaced with this maximum value. In this case, the deflection angle is probably influenced most. If the difference between the two ray-tracing results is indistinguishable, it is unnecessary to calculate the real deflection angle in the simulation.

Figure 4 presents the convergence field obtained from one single realization, in which the color bar represents the convergence (surface mass density). To validate our simulation results, we calculate the shear-shear correlation functions,  $\xi_+$  and  $\xi_-$ , in the  $\Lambda\text{CDM}$  simulation and compare them with the

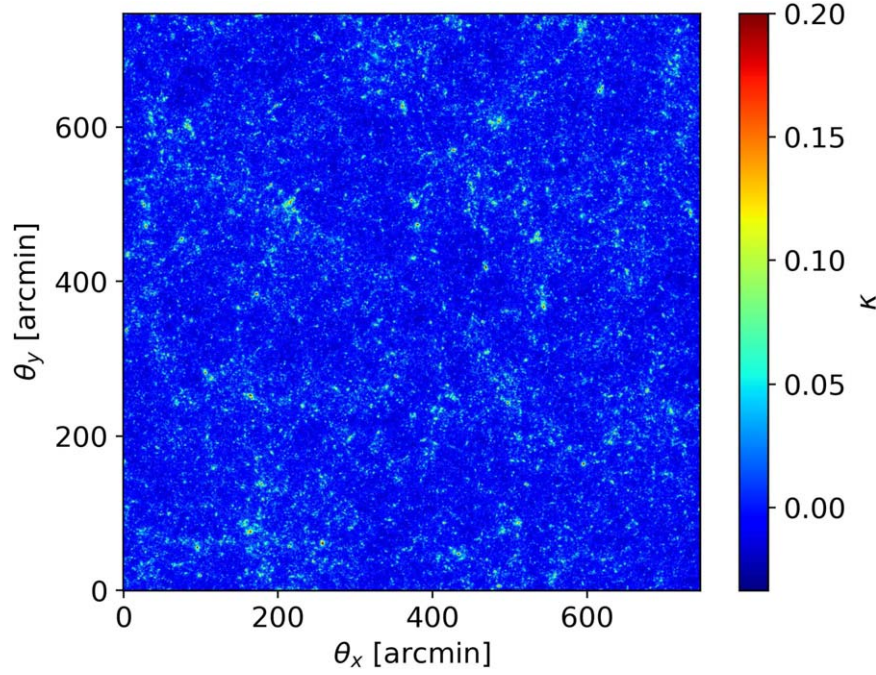


**Figure 4.** The simulated convergence map for one realization based on GR gravity. The color bar represents the amplitude of the convergence.

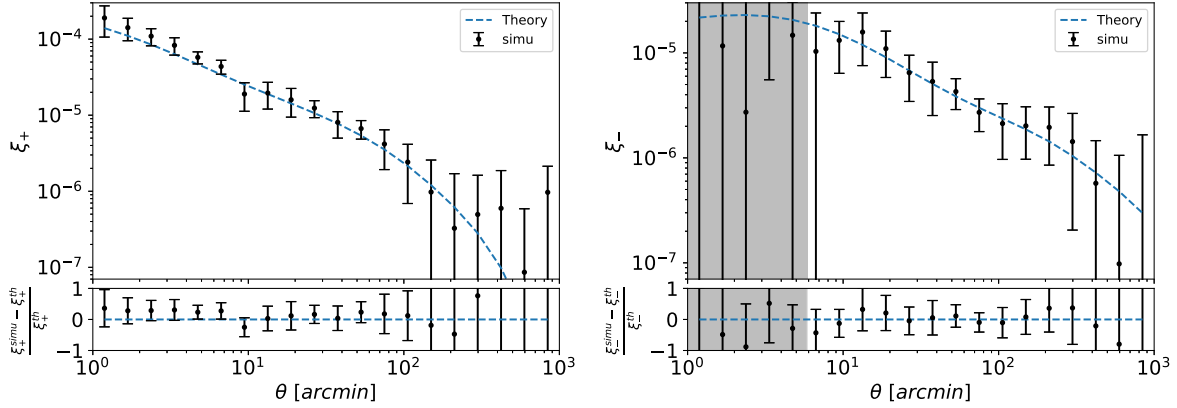


**Figure 5.** Cosmic shear statistics in GR simulation. The left panel shows  $\xi_+$  and the right panel shows  $\xi_-$ . Relative differences between theory and simulation are presented in the bottom panels. The dashed blue line represents the theoretical prediction, and the black dots with error bars represent the measurements from the simulated shear map. The shaded region indicates the smoothed regions by the PM method. One can see that the simulation results agree with the theoretical predictions.

theoretical predictions. We randomly sample 558,282 galaxies (corresponding to a galaxy number density of  $1 \text{ arcmin}^{-2}$ ) and place them down on the surface at a redshift of  $z = 0.75$ , resulting in a uniform distribution of their projected distances. Note that because this is only a test, the population of background galaxies is not expected to be realistic. However, in order to obtain a reliable void catalog, we need to construct a more realistic galaxy catalog because the void finder is sensitive to the foreground galaxy catalog. We therefore use SHAM to populate galaxies in the previous section. We also consider the noisy shear components in the measurement by including a random ellipticity drawn from a Gaussian distribution with a standard deviation of  $\sigma_e = 0.3$  (see Section 4.2). For the theoretical predictions, we use NICERA (Kilbinger et al. 2009) to calculate the theoretical cosmic shear. The nonlinear matter power spectrum model is taken from Takahashi et al. (2012), and the transfer function is taken from Eisenstein & Hu (1998) with baryon acoustic oscillation (BAO) wiggles. The results are exhibited in Figure 5, where the

measurements are obtained by averaging the results from nine light cones. The shaded region marked in  $\xi_-$  indicates the angular scale corresponding to the length of the mesh grid ( $\sim 6'$ ) chosen in the PM algorithm, where the measurements are probably not reliable. In general, the results of our ray-tracing simulation are reliable. It should be noted that we use a different source of the nonlinear power spectrum, but we performed a consistency test and found that the differences between the power spectra obtained from theory and simulation are smaller than 5%, which is smaller than the cosmic variance. Considering the large error bar in Figure 5, this discrepancy due to the usage of a different source of power spectrum does not influence the conclusion of this check.

#### 4. Results

In this section, we present our main results both in theory and simulation. For the theoretical calculations, we used the void profiles measured in Section 3.2. The change in the dark



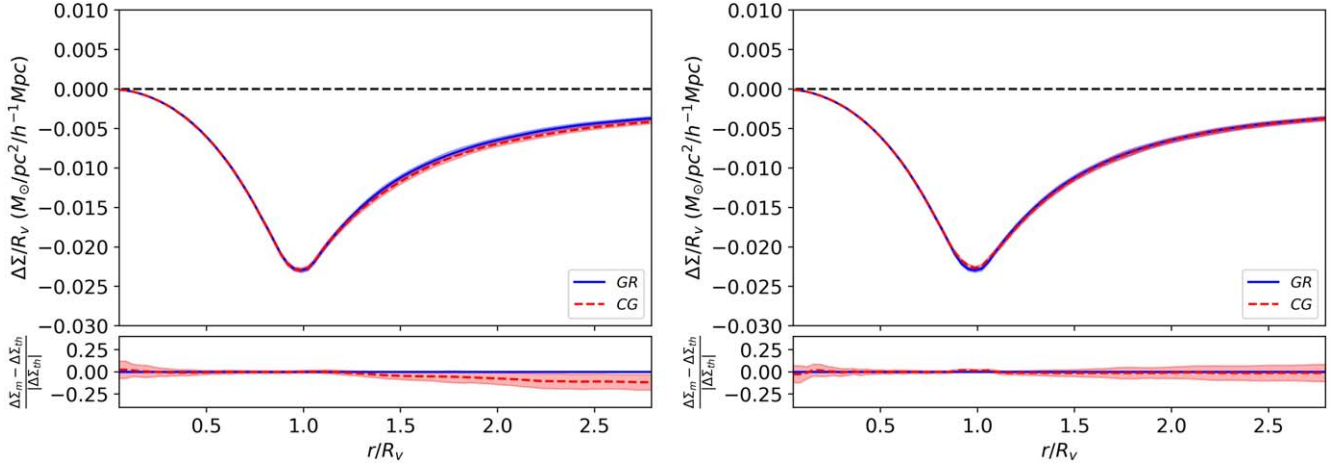


**Figure 6.** Lensing signals calculated in different models. In both panels, the blue lines represent the calculation results of the GR model, and the red lines represent the CG model. The shadow regions represent the error propagated from the jackknife error in void profiles. Left: Impact of the void density profile on the lensing signal in the GR and CG gravity models. Lensing signals were calculated using the same deflection angle (i.e., the same Poisson equation), but different density profiles. Right: Impact of the deflection angle on the lensing signal in two theories. This calculation used the same void density profile, but different Poisson equations for the two gravity models. It can be seen that the discrepancies between these two models are negligible compared with the discrepancy in the left panel, i.e., from the modification of the void profile, illustrating no significant effect from the modification of the Poisson equation.

matter field and the deflection angle are considered separately during the calculation. For the simulation results, we cross-correlated the foreground void position field with the background shear field to obtain the lensing signal. Finally, we analyze the capability of the void lensing effect in distinguishing gravity models.

#### 4.1. Theoretical Lensing Signal

We calculate the ESD based on the GR and CG gravity models described in Section 2.2. During the calculation, we used the open-source package `scipy.fft.fft` (Virtanen et al. 2020) for the Fourier transform and its inverse. Effects from the change in the void profile and the deflection angle are considered separately. First, the effects of different void profiles are investigated. In the left panel of Figure 6, we show the lensing signals around voids in GR and CG simulations, while the lensing signal is calculated with the same deflection angle as predicted in GR. The error bar in the figure is estimated in this way: The jackknife error of the lensing signal is estimated in each single simulation. We then combine these signals and average them to obtain the mean signal while propagating the jackknife error in each realization to the final signal. As shown in the figure, the lensing signal of the CG theory is larger than that of GR (even with a relatively large error bar), which is consistent with the properties in the void profile (Figure 2), where CG voids have an emptier profile. This can be explained by the fifth force, which provides an additional contribution to enhancing the structure formation. Second, the lensing signals are calculated on the same input void profile (from GR), but with different deflection angles adapted for the two gravity models, respectively. The error bar is estimated in the same way as was used in the case that only modifies the dark matter field. Our results are shown in the right panel of Figure 6, showing that the influence of the change in the deflection angle is negligible compared to that of the different density profiles. This is expected because  $G_{\text{eff}}$  differs from  $G$  only on the order of one thousandth (see Figure 5 in Zhang et al. 2020).

Based on these calculations, we can conclude that the CG theory affects the lensing signal mostly by changing the void profile rather than by changing the deflection angle of light, but to a fairly limited extent. It is also expected that in the following simulation results, if one only works on a modified deflection angle, there should be a less distinguishable discrepancy.

#### 4.2. Lensing Signal from a Simulation

We measure the lensing statistics  $\Delta\Sigma$  (ESD) from our ray-tracing simulations. Based on Equations (6) and (9), the ESD can be related to tangential shear  $\gamma_t$  by

$$\Delta\Sigma = \Sigma_{\text{crit}} \gamma_t, \quad (11)$$

where  $\Sigma_{\text{crit}}$  is defined as

$$\Sigma_{\text{crit}} = \frac{1}{4\pi G} \frac{D_A(z_s)}{D_A(z_L)D_A(z_L, z_s)}, \quad (12)$$

where  $D_A$  is the angular diameter distance. The estimator of the ESD,

$$\widehat{\Delta\Sigma} = \frac{\sum_{i,j} w_{ij} e_{t,ij} \Sigma_{\text{crit},ij}}{\sum_{ij} w_{ij}}, \quad (13)$$

where  $e_t$  represents the ellipticity of the background galaxy,  $w$  represents the weight of each source-lens pair, and the summation is made over all source-lens pairs.

We randomly sample 5,582,821 background galaxies (corresponding to a number density of  $10.00 \text{ arcmin}^{-2}$ ) on a source plane located at  $z=0.75$ , rendering their projection positions to satisfy a uniform distribution. Furthermore, each background galaxy is assigned a redshift dispersion of  $\Delta z=0.001$ . In practice, the shear components in the ray-tracing simulation are the ellipticities of background galaxies, while for foreground voids, we select those in slices that constitute the lens plane at  $z=0.3$ , of which the redshifts are determined by their comoving distance to us along the line of sight, but also with a dispersion of  $\Delta z=0.001$ . We employ

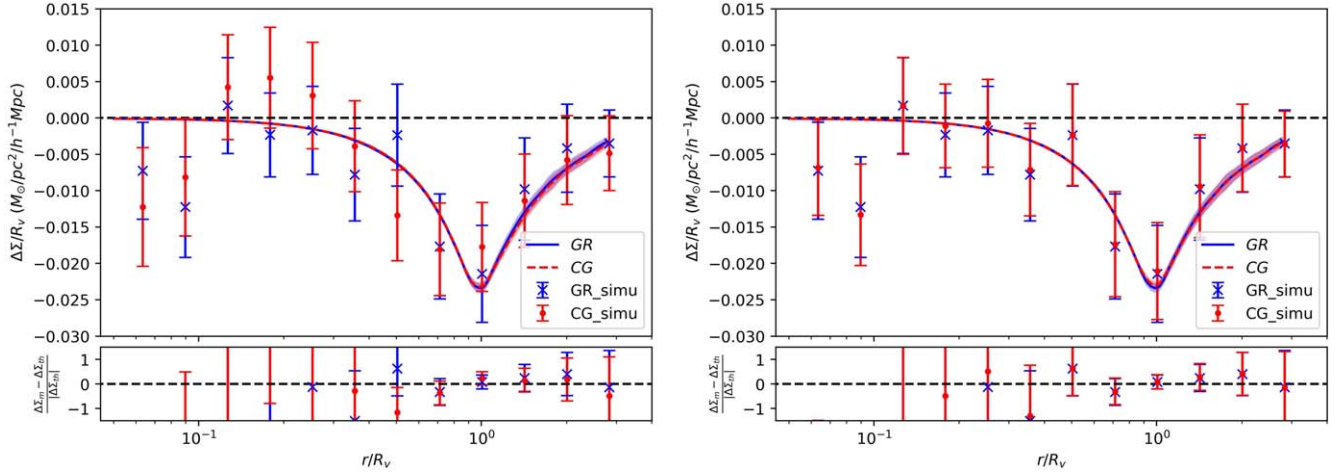


**Figure 7.** ESD measured in a simulation (dots with error bar) vs. theoretical predictions (lines) from the GR and CG. The error bars in both theories and simulations are obtained from the jackknife method. Left: Only the void density profile is changed, representing the effects on the structure formation. The CG model is plotted in red and the GR model in black. It can be seen that the two models are consistent with the corresponding simulation results, but with a large error bar. Right: Only the deflection angle is changed. The void profile is obtained from the GR simulation. In this panel, we only consider an extreme case. It can be seen that consistent with the findings in theoretical predictions, the simulation results of the two models are indistinguishable.

SWOT (Coupon et al. 2012) to measure the ESD around the foreground voids.

Our results for the GR and CG models in comparison are displayed in Figure 7. The left panel is dedicated to the measurement of different dark matter fields, but with the same deflection angle, and vice versa for the right panel. The left panel shows that the lensing signal of the GR is systematically stronger than that of the CG, but the difference is not significant. For the right panel, an expected result shows up because there is no significant deviation for the GR from the CG simulation.

In Section 2.3 we discussed the lensing statistics  $\Delta\Sigma$  and the equivalence between this and the physical excess surface mass density. Since we find that the change to the lensing signal from a varying deflection angle cannot be compared to that from a differing void density profile, it is still valid to interpret the differential projected mass density as the lensing signal here. The discussions below are limited to the case of varying the dark matter density fields alone. Nevertheless, in other MG theories, it may not be such a simple case. That is, our method should be more useful in studying MG theories that can greatly modify the deflection angle.

We are interested in the capability of void lensing statistics in distinguishing different gravity models. The first thing is to reduce the statistical uncertainty. To accomplish this, we employ the same procedure to generate nine background galaxy catalogs and nine corresponding foreground void catalogs from nine light cones. By averaging the resulting lensing signals, we are able to decrease the statistical uncertainty by a factor of one-third relative to a single realization. Our simulation results then represent an observation case with an effective survey area of  $\sim 1395 \text{ deg}^2$ . In order to account for shape noise, we incorporate noisy shear components ( $e_1, e_2$ ) into our measurements, where  $e = (\gamma + n)/(1 + n\gamma^*)$ . Here we use the convention of  $e = e_1 + ie_2$ ,  $\gamma = \gamma_1 + i\gamma_2$  (shear from simulation), and  $n = n_1 + in_2$  (random ellipticity). The random ellipticity components are drawn from a Gaussian distribution with zero mean and a standard deviation of  $\sigma_e = 0.3$ . The results are established in Figure 8.

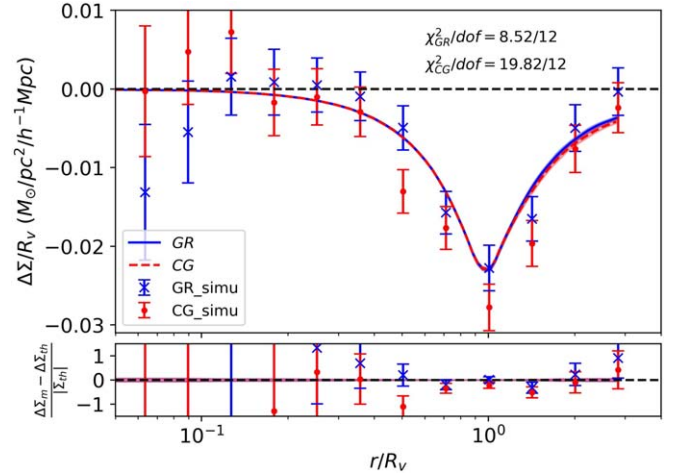


**Figure 8.** The same as Figure 7, but estimated by averaging measurements from nine light cones. We also show the deviation between simulation and theory in the bottom panel. For the theoretical predictions, we calculate the ESD using stacked void profiles in nine light cones and combine these nine results as the final predictions. The jackknife error in each single measurement is combined as the error bar.

Clearly, in Figure 8 the statistical uncertainties for both GR and CG models are significantly reduced. This allows us to assess the capability of void lensing as a probe to detect the discrepancy between GR and CG gravity. We use the GR and CG simulation data separately as the observed signal for a fitting of theoretical predictions. The goodness of fit is manifested in the  $p$ -value. In each simulation, the number of data points is 12, where the number acts as the degree of freedom given no additional free parameters from the two gravity models.

We first assume that the observed signals are consistent with those in the GR simulation, and then calculate the  $\chi^2$  value of the two theoretical predictions. The  $\chi^2$  value of the GR model is 8.52, indicating that the model can be rejected at  $0.33\sigma$ :  $p_{\text{GR}} = 0.744$ . In contrast, the  $\chi^2$  value of the CG model is 8.62, corresponding to a  $p$ -value of 0.735, which implies that the CG model can be rejected at  $0.34\sigma$ . Therefore, we cannot reject the



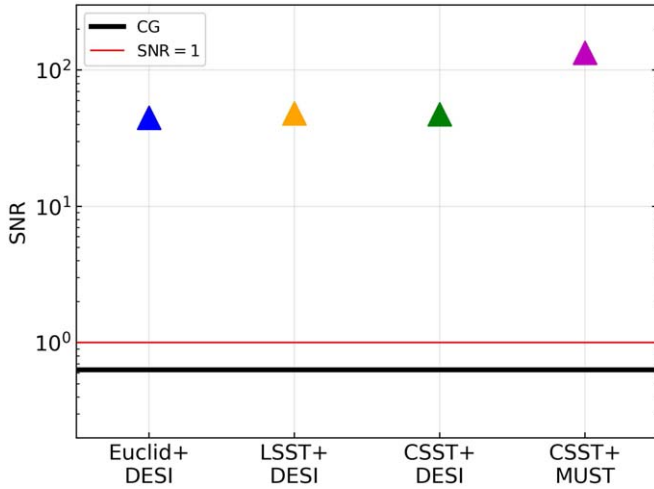


**Figure 9.** Comparison of the S/N of the differences between CG and GR in ESD predicted by different future survey conditions. The solid black line represents S/N in our simulation. The colored triangles represent the S/N of the differences between GR and CG. The different colors represent different combinations of spectroscopic and photometric surveys.

CG model, although the GR model has a lower  $\chi^2$  value than the CG model.

We then assume that the CG simulation represents the real observation and repeat the analysis. The  $\chi^2$  of the GR model is 20.537, corresponding to a  $p$ -value of 0.058. This implies that GR gravity is rejected by the CG simulation at  $1.90\sigma$ . In comparison, the  $\chi^2$  of CG model is 19.823, which is rejected at  $1.81\sigma$  with a  $p$ -value of 0.071. The results present a preference for CG gravity in the CG simulation, but it is not significant because the differences between CG and GR models are much smaller than those between the simulations (see Figure 8). Furthermore, the consistency between CG theory and simulation is lower than expected, which might be due to the simplification of the theoretical model, to an incomplete estimation of the cosmic variance, or to other unknown systematics.

#### 4.3. Forecast for the Next-generation Survey

In the previous subsection, we concluded that the two models are not distinguishable in the case of our simulations. It is interesting to consider whether the next-generation survey will be able to detect differences between these two models. We can make a simple prediction for the probability of distinguishing these two models with the help of the signal-to-noise ratio (S/N), which is defined as

$$S/N = \sum_i \frac{\Delta\Sigma_{CG} - \Delta\Sigma_{GR}}{\sqrt{(\sigma_{i,GR}^2 + \sigma_{i,CG}^2)}}, \quad (14)$$

where  $\Delta\Sigma_i$  is the void lensing signal, and  $\sigma^2$  represents the errors. Here, for the CG model, only the dark matter field is modified. It should be also noted that we ignore the covariance between data points, which will result in an overestimation of the S/N. The solid black line in Figure 9 represents the S/N of our simulation, whose value is  $\sim 0.6$ , indicating that it might be impossible to distinguish these two gravity models (which is consistent with the results in Section 4.2). Then we investigate how the next-generation weak-lensing survey can raise the value of S/N. There are two possible approaches to improving the S/N. The first is to increase the void number density, requiring expanding the spectroscopic survey. In

this forecast, we consider two spectroscopic surveys: DESI (DESI Collaboration et al. 2016), which has a void number density of  $\sim 1 \text{ arcmin}^{-2}$  (we assume that the number of voids is proportional to the number of galaxies, so if the galaxy number density is 10 times greater than in our simulations, the void number density is estimated to be 10 times greater than ours); and the Multiplexed Survey Telescope (MUST),<sup>8</sup> which has an optimally evaluated galaxy number density that is eight times higher than that of DESI, resulting in a corresponding void number density of  $8 \text{ arcmin}^{-2}$ . The second approach to improve the S/N involves increasing the background galaxy number and widening the survey area, which can be achieved by future photometric surveys. Three next-generation survey missions are taken into account: Euclid, LSST, and CSST. Euclid is expected to cover a survey area of  $15,000 \text{ deg}^2$  with a background galaxy number density of  $\sim 30.0 \text{ arcmin}^{-2}$  (Laureijs et al. 2011). LSST, on the other hand, aims to scan  $20,000 \text{ deg}^2$  with a galaxy number density of  $26 \text{ arcmin}^{-2}$  (Chang et al. 2013). Finally, the CSST survey has a total survey area of  $17,500 \text{ deg}^2$  with a galaxy density of  $28.89 \text{ arcmin}^{-2}$  (Gong et al. 2019). Based on the void number density in next-generation spectroscopic surveys, the galaxy number density, and the survey area in the next-generation photometric survey, we present the improved S/N values in Figure 9. The labels on the bottom axis of the figure are formatted as “spec survey” + “photo survey” where, for example, “Euclid + DESI” represents the S/N with the void number density of DESI, a survey area and the background galaxy density of Euclid. As illustrated in the figure, all four cases can increase the S/N value to  $\sim 40$ – $50$ . This suggests that it may be possible to distinguish the CG and GR models in the next-generation survey data. However, it is important to note that our forecast is a simple case and does not consider the dependence of the galaxy bias on the local density. As pointed out in Pollina et al. (2017), the galaxy bias is different in the voids we considered in this paper. Therefore, further efforts are needed to obtain a more accurate evaluation of the possibility of distinguishing these two models by void lensing.

In addition, we also forecast that the effects with respect to the deflection angle can be detected in the next-generation surveys. For this case, the S/N in our simulation is lower than  $10^{-4}$ , and the next-generation survey can only increase the value to about 2 orders of magnitude, which is still far from unity. Therefore, it seems that for the CG gravity studied in this paper, it is unnecessary to run a ray-tracing simulation to obtain the lensing signals. However, we also point out that this conclusion is only valid for the CG gravity considered in our study, and for other gravity models, especially for those in which the deflection angle is greatly changed, it is necessary to run a ray-tracing simulation to check the correction of the lensing signals obtained from the  $N$ -body simulation.

## 5. Summary and Conclusion

In this study, we focused on investigating the weak-lensing signal around cosmic voids in the context of CG gravity, and we further tested whether the effects from the deflection angle in this model can be reliably neglected. Instead of directly projecting the dark matter density field along the line of sight in  $N$ -body simulation, we used a ray-tracing technique to generate

<sup>8</sup> <https://must.astro.tsinghua.edu.cn/must/index.html>

convergence and shear maps on the background at a redshift of  $z = 0.75$ . The foreground mock galaxies at  $z = 0.3$  generated by SHAM and voids are identified from them using the DIVE method, and the background galaxies are randomly sampled from a uniform distribution on a single source plane. The effective survey area in our simulation ( $\sim 1395 \text{ deg}^2$ ) as well as the number of background galaxies ( $10 \text{ arcmin}^{-2}$ ) are chosen so as to match the current KiDS-like weak-lensing survey. The lensing signals are measured from the simulations, which constitute the “real observations” compared with theoretical predictions. Our conclusions are listed below.

- (1) Regarding the void lensing signal, the effect of the CG gravity on the deflection angle cannot be compared to that on the void profile. Owing to a less distinguishable  $G_{\text{eff}}$  from the gravitational constant, the interaction between particles and particles (photons) in CG is very similar to that in GR. Nonetheless, the cumulative effect on the structure formation should still be observable in our simulations, which span from  $z = 49$  to  $z = 0$ . In contrast, the effect on the deflection angle is transient, even when accounting for foreground matter between  $z = 0$  and  $z \sim 1$ , which determines its subordinate status. However, some other studies such as Baker et al. (2018) and Barreira et al. (2015) hold the opposite view, suggesting that the void lensing signals in CG can be approximately twice as strong as in GR due to the change in the lensing potential (i.e., the deflection angle). This difference can be explained by two aspects: (a) the inclusion of a potential term as a source to drive late acceleration in the Lagrangian of our CG model, which is different from the literature; and (b) the prevalent tracker ansatz proposed by de Felice & Tsujikawa (2010) is no longer suitable for our model due to the participation of the potential term. To this end, we employ numerical techniques to solve the autonomous equations while preserving high-order terms in the field equations that were dropped in Barreira et al. (2015).
- (2) For both GR and CG, the measured signals are consistent with the theoretical predictions. Since the lensing signal is barely sensitive to the change in deflection angle, the detection of  $\Delta\Sigma$  can be approximately transferred to a measurement of the foreground void density profile. The theoretical prediction, which is a projection of the 3D density profile, is expected to agree well with the measurement from our ray-tracing simulations. The slight overestimation seems to be spurious and can be attributed to the small box size of the simulation, the number of realizations, and the simplification of the theoretical model. Despite this, our method has two major advantages: (a) It can be used as a test for lensing studies in other MG theories, particularly those with significantly changed deflection angles. This test is crucial to verify Equation (9), i.e., the ESD is an accurate estimation of the lensing potential. (b) The use of ray-tracing techniques to measure the lensing signal from  $N$ -body simulations is more reliable than a direct projection onto the mass density, as the latter lacks the change in the deflection angle and the total distribution of mass between the source and lens.
- (3) The two gravity models are indistinguishable in our work, where the configuration of our simulations is up to an effective survey area of  $\sim 1395 \text{ deg}^2$  and a galaxy number

density of  $10 \text{ arcmin}^{-2}$ . It is possible to distinguish these two models with the help of the extended survey area and enlarged galaxy number density. By analyzing the S/N of the differences between the two gravity models, we find that in the next-generation surveys, the S/N reaches from  $\sim 0.6$  to  $\sim 40\text{--}50$ . However, in the data processing, many other difficulties such as systematic calibrations must be overcome. Meanwhile, the dependence of the galaxy bias on the local density is not considered in the forecast and needs to be modeled more accurately in future work. Additionally, even considering the next-generation survey, the effect due to the modification of the deflection angle cannot be detected either. In other words, in the Stage-IV era, it is still valid to make the approximation that the lensing statistics ESD is the projection of 3D dark matter density in CG gravity. This is expected because the effective gravitational constant  $G_{\text{eff}}$  is very similar to the Newtonian gravitational constant  $G$  in this gravity. We would also like to stress that when studying the lensing effect in the gravity models, especially those in which changes in the deflection angle have a larger influence on the lensing signal than changes in the dark matter field, it is necessary to run a ray-tracing simulation to obtain a more reliable lensing signal.

As a bonus at the end, we would like to stress that measuring the lensing signal from  $N$ -body simulations is feasible via a projected 3D density profile for CG gravity, after a comparison to the use of the ray-tracing technique. This conclusion should be valid in the context of a CG gravity that can appreciably modify the dark matter density field other than the deflection angle. It is a promising algorithm for studying lensing effects in gravity models that apparently modify the path of the photons. A practical test of our method on real data, for example, those from the LSST, Euclid, and the CSST will be of more interest and is left for future works, along with a sophisticated modeling of observational systematics. Additionally, exploring how to distinguish CG gravity from GR through a synergy of void lensing with other observables (e.g., galaxy clustering and galaxy–galaxy lensing), as well as determining the extent to which we can constrain the model, are both worth studying.

### Acknowledgments

We thank the anonymous referee for the valuable comments and suggestions that improved our paper. We would like to thank Bikash R. Dinda, Md. Wali Hossain, and Anjan A. Sen for valuable discussions. C.S. would also like to thank Ningchen Bai for discussions on the theory of modified gravity. We acknowledge the support from the science research grants from the China Manned Space Project with No. CMS-CSST-2021-A01, No. CMS-CSST-2021-A03, No. CMS-CSST-2021-A07, and No. CMS-CSST-2021-B01. H.Y.S. acknowledges the support from the NSFC of China under grant 11973070, the Key Research Program of Frontier Sciences, CAS, grant No. ZDBS-LY-7013, and the Program of the Shanghai Academic/Technology Research Leader. J.Y. and C.Z. acknowledge the support from the SNF 200020\_175751 and 200020\_207379 “Cosmology with 3D Maps of the Universe” research grant. Q.W. acknowledges the support from the National Natural Science Foundation of China (grant No. 11988101). X.K.L. and A.Z. acknowledge the support from the NSFC of China under grant No. 12173033. L.

X. is supported by the National Research Foundation of Korea (NRF) through grant No. 2020R1A2C1005655 funded by the Korean Ministry of Education, Science and Technology (MoEST), and by the faculty research fund of Sejong University. This work made use of the High Performance Computing Resource in the Core Facility for Advanced Research Computing at Shanghai Astronomical Observatory.

### ORCID iDs

Huanyuan Shan  <https://orcid.org/0000-0001-8534-837X>

Jiajun Zhang  <https://orcid.org/0000-0002-4117-343X>

### References

- Abbott, B. P., Abbott, R., Abbott, T. D., et al. 2017a, *PhRvL*, **119**, 161101
- Abbott, B. P., Abbott, R., Abbott, T. D., et al. 2017b, *ApJL*, **848**, L12
- Abbott, B. P., Abbott, R., Abbott, T. D., et al. 2017c, *ApJL*, **848**, L13
- Amon, A., Blake, C., Heymans, C., et al. 2018, *MNRAS*, **479**, 3422
- Babichev, E., & Deffayet, C. 2013, *CQGra*, **30**, 184001
- Baker, T., Clampitt, J., Jain, B., & Trodden, M. 2018, *PhRvD*, **98**, 023511
- Barreira, A., Bose, S., Li, B., & Llinares, C. 2017, *JCAP*, **2017**, 031
- Barreira, A., Cautun, M., Li, B., Baugh, C. M., & Pascoli, S. 2015, *JCAP*, **2015**, 028
- Barreira, A., Li, B., Baugh, C. M., & Pascoli, S. 2013a, *JCAP*, **2013**, 056
- Barreira, A., Li, B., Hellwing, W. A., Baugh, C. M., & Pascoli, S. 2013b, *JCAP*, **2013**, 027
- Barreira, A., Li, B., Sanchez, A., Baugh, C. M., & Pascoli, S. 2013c, *PhRvD*, **87**, 103511
- Behroozi, P. S., Conroy, C., & Wechsler, R. H. 2010, *ApJ*, **717**, 379
- Cai, Y.-C. 2018, *IJMPD*, **27**, 1848007
- Cai, Y.-C., Padilla, N., & Li, B. 2015, *MNRAS*, **451**, 1036
- Cataldi, P., Pedrosa, S., Padilla, N., et al. 2022, *MNRAS*, **515**, 5358
- Cautun, M., Paillas, E., Cai, Y.-C., et al. 2018, *MNRAS*, **476**, 3195
- Chang, C., Jarvis, M., Jain, B., et al. 2013, *MNRAS*, **434**, 2121
- Clampitt, J., & Jain, B. 2015, *MNRAS*, **454**, 3357
- Coupon, J., Kilbinger, M., McCracken, H. J., et al. 2012, *A&A*, **542**, A5
- Crocce, M., Pueblas, S., & Scoccimarro, R. 2006, *MNRAS*, **373**, 369
- Davies, C. T., Cautun, M., & Li, B. 2019, *MNRAS*, **490**, 4907
- de Felice, A., Kase, R., & Tsujikawa, S. 2011, *PhRvD*, **83**, 043515
- de Felice, A., & Tsujikawa, S. 2010, *PhRvL*, **105**, 111301
- DESI Collaboration, Aghamousa, A., Aguilar, J., et al. 2016, arXiv:1611.00036
- Eisenstein, D. J., & Hu, W. 1998, *ApJ*, **496**, 605
- Ezquiaga, J. M., & Zumalacárregui, M. 2017, *PhRvL*, **119**, 251304
- Gannouji, R., & Sami, M. 2010, *PhRvD*, **82**, 024011
- Gong, Y., Liu, X., Cao, Y., et al. 2019, *ApJ*, **883**, 203
- Hilbert, S., Hartlap, J., White, S. D. M., & Schneider, P. 2009, *A&A*, **499**, 31
- Horndeski, G. W. 1974, *IJTP*, **10**, 363
- Hossain, M. W., & Sen, A. A. 2012, *PhLB*, **713**, 140
- Khoury, J., & Weltman, A. 2004a, *PhRvD*, **69**, 044026
- Khoury, J., & Weltman, A. 2004b, *PhRvL*, **93**, 171104
- Kilbinger, M., Benabed, K., Guy, J., et al. 2009, *A&A*, **497**, 677
- Knollmann, S. R., & Knebe, A. 2011, AHF: Amiga's Halo Finder, Astrophysics Source Code Library, ascl:1102.009
- Kobayashi, T. 2019, *RPPh*, **82**, 086901
- Kravtsov, A. V., Berlind, A. A., Wechsler, R. H., et al. 2004, *ApJ*, **609**, 35
- Laureijs, R., Amiaux, J., Arduini, S., et al. 2011, arXiv:1110.3193
- Liao, S. 2018, *MNRAS*, **481**, 3750
- Melchior, P., Sutter, P. M., Sheldon, E. S., Krause, E., & Wandelt, B. D. 2014, *MNRAS*, **440**, 2922
- Nesseris, S., de Felice, A., & Tsujikawa, S. 2010, *PhRvD*, **82**, 124054
- Nicolis, A., Rattazzi, R., & Trincherini, E. 2009, *PhRvD*, **79**, 064036
- Paillas, E., Cautun, M., Li, B., et al. 2019, *MNRAS*, **484**, 1149
- Perico, E. L. D., Voivodic, R., Lima, M., & Mota, D. F. 2019, *A&A*, **632**, A52
- Pollina, G., Hamaus, N., Dolag, K., et al. 2017, *MNRAS*, **469**, 787
- Renk, J., Zumalacárregui, M., Montanari, F., & Barreira, A. 2017, *JCAP*, **2017**, 020
- Schneider, P. 2006, in Saas-Fee Advanced Course 33: Gravitational Lensing: Strong, Weak and Micro, ed. G. Meylan, P. Jetzer, & P. North (Berlin: Springer), **1**
- Takahashi, R., Sato, M., Nishimichi, T., Taruya, A., & Oguri, M. 2012, *ApJ*, **761**, 152
- Vainshtein, A. I. 1972, *PhLB*, **39**, 393
- Virtanen, P., Gommers, R., Oliphant, T. E., et al. 2020, *NatMe*, **17**, 261
- Wilson, C., & Bean, R. 2021, *PhRvD*, **104**, 023512
- Yu, J., Zhao, C., Chuang, C.-H., et al. 2022, *MNRAS*, **516**, 57
- Zhang, J., An, R., Liao, S., et al. 2018, *PhRvD*, **98**, 103530
- Zhang, J., Dinda, B. R., Hossain, M. W., Sen, A. A., & Luo, W. 2020, *PhRvD*, **102**, 043510
- Zhao, C., Chuang, C.-H., Bautista, J., et al. 2021, *MNRAS*, **503**, 1149
- Zhao, C., Tao, C., Liang, Y., Kitaura, F.-S., & Chuang, C.-H. 2016, *MNRAS*, **459**, 2670
- Zhao, C., Variu, A., He, M., et al. 2022, *MNRAS*, **511**, 5492
- Zumalacárregui, M. 2020, *PhRvD*, **102**, 023523